The dynamics of a vesicle in simple shear flow

HONG ZHAO[1]† AND ERIC S. G. SHAQFEH[1,2]

[1]Department of Mechanical Engineering, Stanford University, Stanford, CA 94305, USA
[2]Department of Chemical Engineering, Stanford University, Stanford, CA 94305, USA

We have performed direct numerical simulation (DNS) of a lipid vesicle under Stokes flow conditions in simple shear flow. The lipid membrane is modelled as a two-dimensional incompressible fluid with Helfrich surface energy in response to bending deformation. A high-fidelity spectral boundary integral method is used to solve the flow and membrane interaction system; the spectral resolution and convergence of the numerical scheme are demonstrated. The critical viscosity ratios for the transition from tank-treading (TT) to 'trembling' (TR, also called VB, i.e. vacillating-breathing, or swinging) and eventually 'tumbling' (TU) motions are calculated by linear stability analysis based on this spectral method, and are in good agreement with perturbation theories. The effective shear rheology of a dilute suspension of these vesicles is also calculated over a wide parameter regime. Finally, our DNS reveals a family of time-periodic and off-the-shear-plane motion patterns where the vesicle's configuration follows orbits that resemble but are fundamentally different from the classical Jeffery orbits of rigid particles due to the vesicle's deformability.

Key words: boundary integral methods, capsule/cell dynamics, suspensions

1. Motivation

A vesicle is a viscous droplet enclosed by a lipid bilayer, which behaves like a two-dimensional *incompressible* fluid in that it admits relative in-plane shear motion without incurring any residual shear stress. The lipid bilayer exhibits resistance to bending deformation because of the coupling between the inner and outer layers. The simplest surface energy model, assuming a homogeneous bilayer structure and zero spontaneous curvature, has the following functional form (Helfrich 1973)

$$W = \int_D 2\kappa H^2 \, \mathrm{d}A + \int_D \sigma \, \mathrm{d}A, \tag{1.1}$$

where D is the vesicle surface, κ is the bending modulus of the lipid bilayer and H is the surface mean curvature. Surface tension σ is in effect a *local* Lagrange multiplier stemming from the surface incompressibility constraint. In contrast, the fluid interface of a regular droplet does not conserve area when deforming, and its surface tension is a basic physical quantity instead of a constraint force. Since the vesicle's volume V and surface area A are both constant, its non-sphericity is measured by the non-dimensional effective volume $v = 3V/(4\pi a^3)$ where $a = \sqrt{A/4\pi}$ is the characteristic length scale. An equivalent measure is the excess area $\Delta = A/(3V/4\pi)^{2/3} - 4\pi$ that is

---

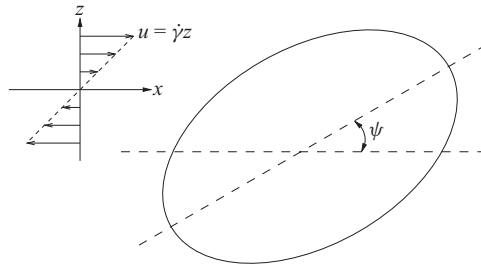† Email address for correspondence: hongzhao@stanford.edu

FIGURE 1. Schematics of a vesicle in a simple shear flow.

related to v by $\Delta = 4\pi(v^{-2/3} - 1)$. Without flow-induced deformation, the equilibrium shape of the vesicle is solely determined by the parameter v.

Figure 1 shows the system of a vesicle immersed in an unbound simple shear flow. The unperturbed velocity field is $u = \dot{\gamma}z$ where $\dot{\gamma}$ is the shear rate. Other relevant physical quantities are non-dimensionalized by the vesicle size a, the bending modulus κ and the external fluid viscosity μ_{out}. The non-dimensional flow shear rate χ and the internal fluid viscosity are, therefore,

$$\chi = \frac{\mu_{out}a^3\dot{\gamma}}{\kappa} \quad \text{and} \quad \lambda = \frac{\mu_{in}}{\mu_{out}}. \tag{1.2}$$

We note that χ is also defined as the capillary number Ca in some references (Danker et al. 2007; Vlahovska & Gracia 2007). This system is fully characterized by the three non-dimensional parameters v, χ and λ.

The classic Keller–Skalak theory (Keller & Skalak 1982) for capsules considers the torque balance and energy dissipation budget, while ignoring the mechanical properties of the capsule membrane by prescribing an ellipsoidal capsule shape. The theory predicts two flow regimes: a steady-state tank-treading (TT) regime where the shape of the vesicle does not change in time and a tumbling (TU) regime where the shape contour precesses around the flow vorticity direction more like a rigid particle. The transition between the two regimes occurs at a critical viscosity ratio λ_c, beyond which the vesicle tumbles. The flow shear rate is a scaling factor for TT and TU frequencies, but does not affect transition.

In flow experiments, the TT and TU of vesicles are both observed, as well as an intermediate 'trembling' (TR) state where the orientation of the vesicle's major axis oscillates (or swings) about the x-axis with small amplitude and the shape contour never makes a full 360° rotation during the motion cycle (Kantsler & Steinberg 2006; Mader et al. 2006; Deschamps, Kantsler & Steinberg 2009). While we adhere to the term 'trembling' for this intermediate state, other names such as 'vacillating-breathing (VB)' (Misbah 2006) or 'swinging' (Noguchi & Gompper 2007) have also been used.

Several small-deformation perturbation theories have been developed for the reduced-order ordinary differential equations of the motion (Misbah 2006; Danker et al. 2007; Lebedev, Turitsyn & Vergeles 2007; Noguchi & Gompper 2007; Vlahovska & Gracia 2007; Kaoui, Farutin & Misbah 2009; Messlinger et al. 2009). The qualitative phase transition behaviour is correctly predicted by these theories: the vesicle undergoes a direct TT to TU transition when $\lambda = \lambda_c$ at a low shear rate, while at a high shear rate the TT to TR transition happens first and the vesicle starts to tumble as λ increases further. These perturbation theories, by expanding the surface

radius up to second-degree spherical harmonics, result in a system of only two degrees of freedom. For leading-order perturbation analysis, the dynamics can be completely described by two parameters S and Λ that combine the effect of v, χ and λ (Lebedev *et al.* 2007). Quantitatively, these perturbation theories severely underpredict the λ_c value compared to experiments (Deschamps *et al.* 2009; Zabusky *et al.* 2010), and a possible cause of the discrepancy is the inadequacy of the second-degree harmonic expansion. A recently developed perturbation theory, by expanding the radius up to fourth-degree spherical harmonics, predicts λ_c values that are almost twice that predicted using second-degree expansions (Farutin, Biben & Misbah 2010).

For numerical simulations, Kraus *et al.* pioneered using a Stokes-flow boundary integral method to simulate the TT of vesicles at $\lambda = 1$ (Kraus *et al.* 1996). Even with the rather crude approximation of calculating the bending energy using the dihedral angle between adjacent triangular surface elements, their simulation correctly predicts important phenomena – among these are the dependence of the TT inclination angle on v and its insensitivity to χ at a high shear rate. High-order boundary integral methods with spectral surface resolution have more recently been developed for simulating model vesicles in two-dimensional space (Freund 2007; Veerapaneni *et al.* 2009*a*), axisymmetric vesicles in three dimensions (Veerapaneni *et al.* 2009*b*) and fully three-dimensional motions of vesicles/capsules (Zhao *et al.* 2010; Veerapaneni *et al.* 2011). Other numerical methods such as multi-particle collision dynamics (Noguchi & Gompper 2007; Messlinger *et al.* 2009), phase field methods (Biben, Kassner & Misbah 2005; Ghigliotti, Biben & Misbah 2010) and immersed boundary methods (Kim & Lai 2010) have also been applied to vesicle simulation with success. A recent simulation work by Biben, Farutin & Misbah (2009) is reported to be in good agreement with the perturbation theory using high-degree spherical harmonics (Farutin *et al.* 2010); however, the details of the numerical scheme are not reported except that it is based on boundary integral equations and appears to be using a triangular surface mesh.

In this study, a spectral boundary integral equation method, similar in many aspects to that used for simulating red blood cells (Zhao *et al.* 2010), is developed to determine the vesicle motion. Besides its ability to perform direct numerical simulation (DNS) of the time-dependent motion of the vesicle at all flow regimes with high fidelity, the formulation used here also makes it possible to directly solve the steady TT state by Newton–Raphson method. This enables us to perform rigorous linear stability analysis of the TT state to determine the λ_c values at the TT-to-TR/TU transition. Our convergent numerical results are in good agreement with the perturbation theories using fourth-degree harmonic expansion, thereby confirming that λ_c is severely underpredicted by theories using second-degree expansion.

The particle shear viscosity and normal stress differences at different flow regimes are systematically studied. We decompose the particle stress into parts that originate from distinct physical sources, and investigate the dependence of each part on the flow parameters and on vesicle configuration, from which we come to the physical explanation for the occurrence of a local minimum in the shear viscosity with the increase of λ. The comparison with theories (Danker & Misbah 2007; Danker *et al.* 2007; Vlahovska & Gracia 2007) and two-dimensional simulation (Ghigliotti *et al.* 2010) shows important differences in the prediction of the normal stress differences, especially the second normal stress difference.

In the following, we discuss the numerical scheme in §2 and present our results in §3. A summary and outlook for future work are given in §4.

2. Spectral boundary integral method

The vesicle surface is mapped from a unit reference sphere and is parameterized by spherical angles (θ, ϕ). Because of the membrane fluidity, we treat the vesicle surface in an Eulerian frame so that the surface coordinate in the Euclidean space is $x = (r \sin\theta \cos\phi, r \sin\theta \sin\phi, r \cos\theta)$, and hence the instantaneous shape is solely determined by the radius function $r = r(\theta, \phi; t)$. This representation is thus similar to that used in small-deformation perturbation analysis (Seifert 1999), and is restricted to shapes whose surface radius is single-valued at any radial direction from the origin, which is the case in the present analysis since the vesicles considered have small to moderate excess area and are not too far from spherical.

Alternatively, we can treat each Cartesian coordinate as an independent function of (θ, ϕ) without additionally requiring (θ, ϕ) to be the orientation angles in the physical space. The added flexibility will be useful at very large excessive area when the vesicle can exhibit complex non-convex shapes. However, this representation has excessive redundancies: the mesh admits free in-plane deformation without changing the shape of the surface that it represents. For linear stability analysis, this will introduce a large number of parasitic eigenmodes representing in-plane surface deformation, which will be difficult to identify. On the other hand, in the representation herein, the coordinates of the origin in the Euclidean space constitute the only degrees of freedom, which can easily be eliminated by, for example, requiring the origin to be the centre of mass of the vesicle.

The parameter space $\{(\theta, \phi) \mid 0 \leqslant \theta \leqslant \pi, 0 \leqslant \phi \leqslant 2\pi\}$ is discretized by a structured mesh, with mesh points being Gauss–Legendre quadrature points in θ and uniform in ϕ. All other surface quantities are discretized on the same mesh. In the following discussions, we use the alternative notation (ξ^1, ξ^2) in place of (θ, ϕ) for tensor calculus on the surface. The radius is approximated by a truncated spherical harmonic expansion,

$$r(\theta, \phi) = \sum_{l=0}^{N} \sum_{m=-l}^{l} \hat{r}_{lm} \bar{P}_{lm}(\cos\theta)\, e^{im\phi}, \tag{2.1}$$

where $\bar{P}_{lm}$ are the normalized associated Legendre functions of orthogonality

$$\int_{-1}^{1} \bar{P}_{lm}(x) \bar{P}_{l'm}(x)\, dx = \delta_{ll'}.$$

The surface has tangents and unit normal

$$a_{1,2} = \frac{\partial x}{\partial \xi^{1,2}} \qquad n = \frac{a_1 \times a_2}{|a_1 \times a_2|}, \tag{2.2}$$

and metric tensor g and curvature tensor b

$$g_{\alpha\beta} = a_\alpha \cdot a_\beta \qquad b_{\alpha\beta} = \frac{\partial a_\alpha}{\partial \xi^\beta} \cdot n, \tag{2.3}$$

where we denote covariant tensor components by subscript and contravariant components by superscript following the standard tensor calculus notation. The mean curvature is $H = \frac{1}{2} b_\alpha^\alpha = \frac{1}{2} g^{\alpha\beta} b_{\alpha\beta}$ and the Gauss curvature $K = b_1^1 b_2^2 - (b_1^2)^2$. The surface derivatives in those quantities are calculated with spectral accuracy using the SPHEREPACK library (Adams & Swarztrauber 1997; Swarztrauber & Spotz 2000).

The surface velocity of a vesicle in an otherwise unperturbed non-dimensional shear flow $u^\infty(x) = (\chi z, 0, 0)$ is solved via a boundary integral formulation (Rallison

& Acrivos 1978; Pozrikidis 1992),

$$\frac{1+\lambda}{2}\boldsymbol{u} - \frac{1-\lambda}{8\pi}\boldsymbol{Ku} + \frac{1}{8\pi\mu}\boldsymbol{N}\,[\![\boldsymbol{f}]\!] = \boldsymbol{u}^{\infty}, \tag{2.4}$$

where μ is the external fluid viscosity (and is unity by our non-dimensionalization), and $[\![\boldsymbol{f}]\!]$ is the total hydrodynamic force acting on the lipid bilayer. $\boldsymbol{N}$ and $\boldsymbol{K}$ are the single-layer and double-layer operators of the free space Stokes flow,

$$(\boldsymbol{N}\boldsymbol{\psi})_j(\boldsymbol{x}_0) = \int_D \psi_i(\boldsymbol{x})G_{ij}(\boldsymbol{x}, \boldsymbol{x}_0)\,\mathrm{d}A(\boldsymbol{x}) \tag{2.5}$$

$$(\boldsymbol{K}\boldsymbol{\psi})_j(\boldsymbol{x}_0) = \int_D \psi_i(\boldsymbol{x})T_{ijk}(\boldsymbol{x}, \boldsymbol{x}_0)n_k(\boldsymbol{x})\,\mathrm{d}A(\boldsymbol{x}), \tag{2.6}$$

where the Green's functions $\boldsymbol{G}$ (Stokeslet) and $\boldsymbol{T}$ (stresslet) are

$$G_{ij}(\boldsymbol{x}, \boldsymbol{x}_0) = \frac{\delta_{ij}}{r} + \frac{\hat{x}_i\hat{x}_j}{r^3} \quad T_{ijk}(\boldsymbol{x}, \boldsymbol{x}_0) = -6\frac{\hat{x}_i\hat{x}_j\hat{x}_k}{r^5} \tag{2.7}$$

with $\hat{\boldsymbol{x}} = \boldsymbol{x} - \boldsymbol{x}_0$ and $r = |\hat{\boldsymbol{x}}|$.

The surface force $[\![\boldsymbol{f}]\!]$ consists of a bending force $\boldsymbol{f_B}$ and a constraint force $\boldsymbol{f_\sigma}$. These are the first variation of the bending and surface tension energy in (1.1),

$$\boldsymbol{f_B} = 2\kappa[2(H^3 - HK) + \Delta H]\boldsymbol{n} \tag{2.8a}$$

$$\boldsymbol{f_\sigma} = -2H\sigma\boldsymbol{n} - \sigma_{,\beta}\boldsymbol{a}^\beta, \tag{2.8b}$$

where $\Delta H = (g^{\alpha\beta}\sqrt{g}H_{,\alpha})_{,\beta}\sqrt{g}$ is the surface Laplace of H.

The surface incompressibility constraint, in the Eulerian frame, dictates zero divergence of surface velocity,

$$0 = \boldsymbol{u}_{,\beta} \cdot \boldsymbol{a}^\beta. \tag{2.9}$$

Equations (2.4) and (2.9) can be jointly written in the matrix form

$$\begin{pmatrix} \boldsymbol{A}_{uu} & \boldsymbol{A}_{u\sigma} \\ \boldsymbol{A}_{\sigma u} & \boldsymbol{0} \end{pmatrix} \begin{pmatrix} \boldsymbol{u} \\ \sigma \end{pmatrix} = \begin{pmatrix} \boldsymbol{b}_u \\ 0 \end{pmatrix}, \tag{2.10}$$

where

$$\boldsymbol{A}_{uu}\boldsymbol{u} = \frac{1+\lambda}{2}\boldsymbol{u} - \frac{1-\lambda}{8\pi}\boldsymbol{Ku} \tag{2.11}$$

$$\boldsymbol{A}_{u\sigma}\sigma = \frac{1}{8\pi\mu}\boldsymbol{N}\boldsymbol{f_\sigma} \tag{2.12}$$

$$\boldsymbol{A}_{\sigma u}\boldsymbol{u} = \boldsymbol{u}_{,\beta} \cdot \boldsymbol{a}^\beta \tag{2.13}$$

$$\boldsymbol{b}_u = \boldsymbol{u}^{\infty} - \frac{1}{8\pi\mu}\boldsymbol{N}\boldsymbol{f_B}. \tag{2.14}$$

The surface tension σ is solved by inverting the Schur complement of $\boldsymbol{A}_{uu}$ and the solution of $\boldsymbol{u}$ follows,

$$\boldsymbol{A}_{uu}\boldsymbol{u}^* = \boldsymbol{b}_u \tag{2.15}$$

$$(\boldsymbol{A}_{\sigma u}\boldsymbol{A}_{uu}^{-1}\boldsymbol{A}_{u\sigma})\sigma = \boldsymbol{A}_{\sigma u}\boldsymbol{u}^* \tag{2.16}$$

$$\boldsymbol{A}_{uu}\boldsymbol{u} = \boldsymbol{b}_u - \boldsymbol{A}_{u\sigma}\sigma, \tag{2.17}$$

where $\boldsymbol{u}^*$ is an intermediate unconstrained surface velocity. The discretized equations

are solved by the matrix-free GMRES method (Saad & Schultz 1986), and the matrix–vector multiplication during each iteration is carried out by computing the surface integrals without explicitly forming the matrix. To evaluate the boundary integrals (2.5) and (2.6) with the singular Green's functions, we first rotate the reference sphere so that its north pole is aligned with x_0 and then use Gauss quadrature in the transformed θ coordinate and trapezoidal rule in ϕ (Zhao *et al.* 2010). The $O(|x - x_0|^{-1})$ singularity in both integrals is cancelled by the $\sin\theta$ factor in the Jacobian and the numerical quadrature converges at its desired rate.

For time-dependent simulations, a relative L_2 error tolerance is set to be 10^{-3} when solving (2.16), and the resulting in-plane velocity divergence is of comparable magnitude; the tolerance is 10^{-4} for the inner loop GMRES iteration that inverts A_{uu}. While no pre-conditioning is used, we have not experienced any matrix ill-conditioning. At $\lambda = 8$, it usually takes 6–8 GMRES iterations to invert A_{uu}, and the outer loop converges after only 2–3 iterations when the most recent σ solution is used for initial guess.

The vesicle surface is evolved for each mesh point as follows:

$$\frac{\partial r}{\partial t} = \frac{\mathrm{D}r}{\mathrm{D}t} - \frac{\partial r}{\partial \theta}\frac{\mathrm{D}\theta}{\mathrm{D}t} - \frac{\partial r}{\partial \phi}\frac{\mathrm{D}\phi}{\mathrm{D}t}. \tag{2.18}$$

The material derivatives $\mathrm{D}(\cdot)/\mathrm{D}t$ are calculated by

$$\frac{\mathrm{D}r}{\mathrm{D}t} = e_r \cdot u \qquad \frac{\mathrm{D}\theta}{\mathrm{D}t} = \frac{e_\theta \cdot u}{r} \qquad \frac{\mathrm{D}\phi}{\mathrm{D}t} = \frac{e_\phi \cdot u}{r \sin\theta}, \tag{2.19}$$

where $e_{r,\theta,\phi}$ are the unit tangents of the spherical coordinate system in $\mathbb{R}^3$.

In our simulations, the surface is discretized by 32×64 mesh points in physical space. The cutoff wavenumber N for the spherical harmonic expansion of r in (2.1) is much smaller (usually 8), and $\partial r/\partial t$ is filtered to degree N for surface evolution. The high filtering ratio is applied to overcome the strong aliasing error in bending force that depends on the fourth-order derivatives of r and is a highly nonlinear functional of deformation. In §3.1, the bending force is shown to have a wider spectrum than r, but is well resolved by the fine surface mesh.

3. Results

3.1. *Steady-state tank-treading solution*

Because of the symmetry of the external flow, the steady TT shape is symmetric about the origin and x–z plane so has a reduced form of expansion

$$r = \sum_{l=0}^{N} \sum_{m=0}^{l} a_{lm} \bar{P}_{lm}(\cos\theta) \cos m\phi \qquad l \text{ be even}, \tag{3.1}$$

where the coefficients a_{lm} are real. Let a be the vector comprised of all a_{lm} coefficients in (3.1); its change rate $\dot{a}$ only depends on a due to the absence of inertia. The TT shape thus satisfies the nonlinear equation $\dot{a}(a) = 0$, and is solved directly by a Newton–Raphson method. To ensure that the Newton iteration results in the specified surface area and volume, the equation is augmented by two Lagrange multipliers λ_A
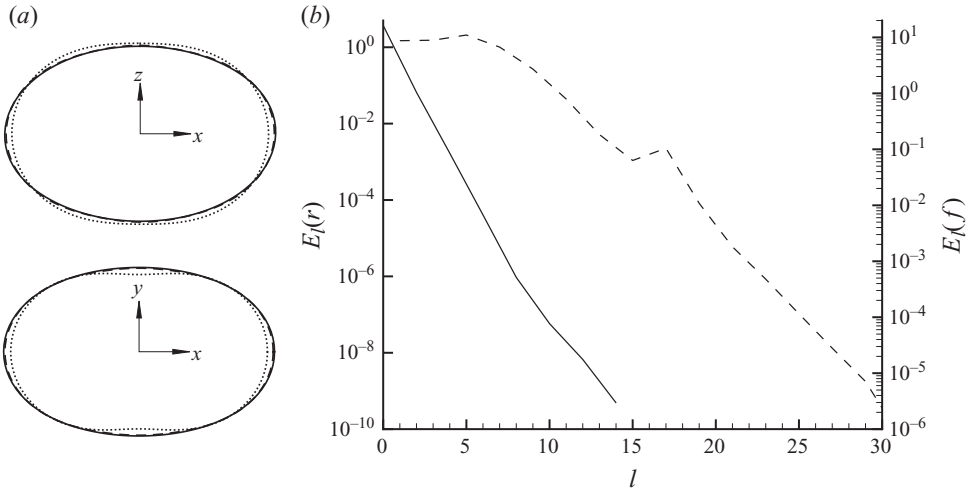
FIGURE 2. A TT vesicle at $v = 0.95$, $\lambda = 8$ and $\chi = 10$. (*a*) Contours obtained with degree of harmonic expansion $N = 2$ ($\cdots\cdots$), $N = 4$ (----) and $N = 14$ (——). (*b*) The energy spectrum of the radius (——) and the bending force (----).

and λ_V,

$$\dot{\boldsymbol{a}} - \lambda_A \frac{\partial A}{\partial \boldsymbol{a}} - \lambda_V \frac{\partial V}{\partial \boldsymbol{a}} = 0 \tag{3.2}$$

$$A = 4\pi \tag{3.3}$$

$$V = \frac{4}{3}\pi v. \tag{3.4}$$

The sub-block $\boldsymbol{M} = \partial\dot{\boldsymbol{a}}/\partial\boldsymbol{a}$ of the Jacobian matrix is computed numerically, with each column obtained by solving $\dot{\boldsymbol{a}}$ with the corresponding a_{lm} perturbed and then using finite difference. A tight error tolerance 10^{-6} is used for solving (2.16) every time, and the tolerance is 10^{-7} for the inner-loop GMRES iteration. The gradient vectors $\partial A/\partial\boldsymbol{a}$ and $\partial V/\partial\boldsymbol{a}$ are calculated similarly.

Solutions at $v = 0.95$ and 0.9 are obtained with N ranging from 2 to 14, while the same 32×64 surface mesh is used in the physical space. Figures 2 and 3 show the shape projections on the x–z and x–y planes at (i) $v = 0.95$, $\lambda = 8.0$, $\chi = 10$; (ii) $v = 0.9$, $\lambda = 6.5$, $\chi = 10$. At the λ values chosen here, the major axes are almost parallel to the x-axis, indicating that the TT state is unstable (or nearly unstable). At $v = 0.95$, the $N = 2$ expansion predicts a non-convex surface contour; for $N \geqslant 4$ the qualitatively correct convex contours are obtained and (for $N \geqslant 4$) shapes of different resolutions are not visibly discernible unless superimposed. The deformation is more profound at $v = 0.9$, but again even the two shapes at $N = 4$ and 14 are not qualitatively different.

Also shown in figures 2 and 3 are the energy spectrum for the surface shape and bending force. We define the modal energy of the surface shape at the latitudinal wavenumber l to be

$$E_l(r) = \sum_{m=-l}^{l} |\hat{r}_{lm}|^2 \tag{3.5}$$

and similarly define $E_l(f)$ for the bending force. The $E_l(r)$ decays exponentially with l in both cases as expected, demonstrating a monotonically diminishing contribution
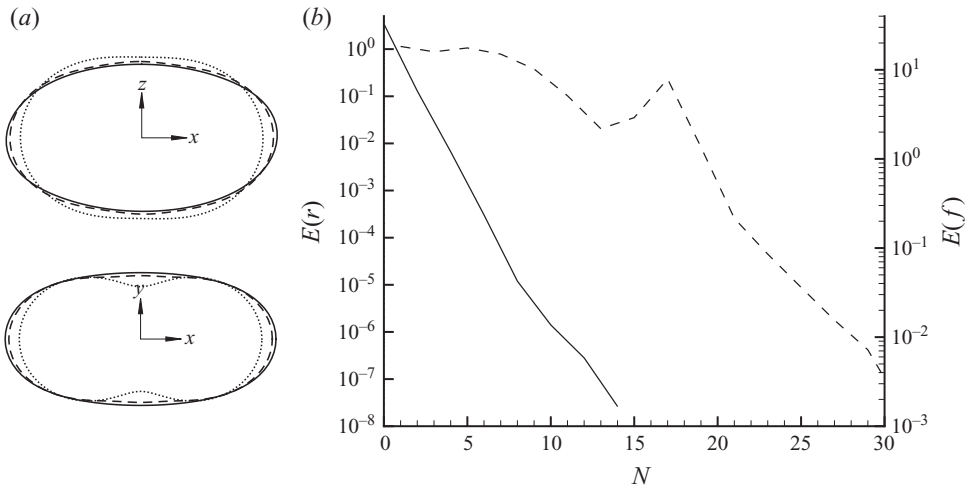
FIGURE 3. TT at $v = 0.9$, $\lambda = 6.5$ and $\chi = 10$. (a) Contours obtained with degree of harmonic expansion $N = 2$ ($\cdots\cdots$), $N = 4$ (-----) and $N = 14$ (———). (b) The energy spectrum of the radius (———) and the bending force (-----).

to surface shape from higher spherical modes. On the other hand, since the bending force depends on the fourth-order surface derivatives of r, the spectrum is wider and the exponential decay starts at larger values of l. At $v = 0.9$, a local peak in $E_l(f)$ occurs at $l = 16$ beyond the cutoff wavenumber of r. With the fine surface mesh resolution in physical space, the bending force is well resolved and filtering the bending force is not necessary here.

The state of the vesicle is described by two important parameters: the inclination angle ψ and a factor D. For a strictly ellipsoidal vesicle, ψ is the angle between the x-axis and the vesicle's longer axis in the x–z plane, and $D = (L_1 - L_2)/(L_1 + L_2)$, where $L_{1,2}$ are the lengths of the longer and shorter axes in the x–z plane. The ratios between the three axial lengths are hence completely determined by v and D. For perturbation theories that expand the radius to second-degree spherical harmonics, ψ and D are the only degrees of freedom of the in-plane motion, and so the system is governed by only two ODEs. Since the shape obtained by our DNS is in general not ellipsoidal, there is not a unique way of defining ψ and D. We choose to identify the three principle axes with the orthogonal eigenvectors of the surface's momentum of inertia tensor $I = \int_D (|\mathbf{x}|^2 \mathbf{I} - \mathbf{x} \otimes \mathbf{x}) \, dA$. The length of each axis is then calculated as the sum of the two radii along the principle axis (plus and minus directions), and the inclination angle is that from the x-direction to the longer principle axis in x–z plane. For a vesicle shape close to ellipsoidal, the difference between the definition used here and that by first fitting the vesicle's shape to an ellipsoid is negligible.

The inclination angle in the TT regime, as predicted by leading-order perturbation theory (Misbah 2006), has the analytical formula

$$\psi = \frac{1}{2} \cos^{-1} \left[\frac{(23\lambda + 32)}{120} \sqrt{\frac{15\Delta}{2\pi}} \right]. \tag{3.6}$$

Therefore, the major axis is along the strain direction ($\psi = \pi/4$) when the vesicle is nearly spherical ($\Delta \ll 1$), and will be more aligned towards the x-axis with increasing non-sphericity and internal viscosity. Equation (3.6) based on the leading-order
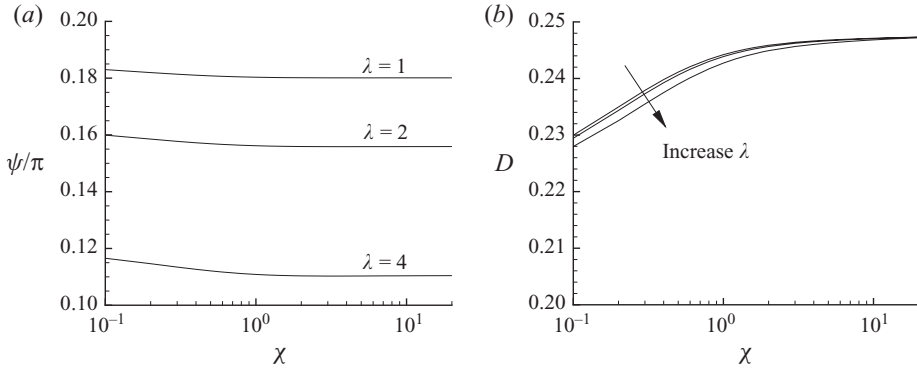
FIGURE 4. The dependence of the inclination angle ψ and deformation factor D of a $v = 0.95$ vesicle on the shear rate χ. Three different viscosity ratios $\lambda = 1$, 2 and 4 are considered.
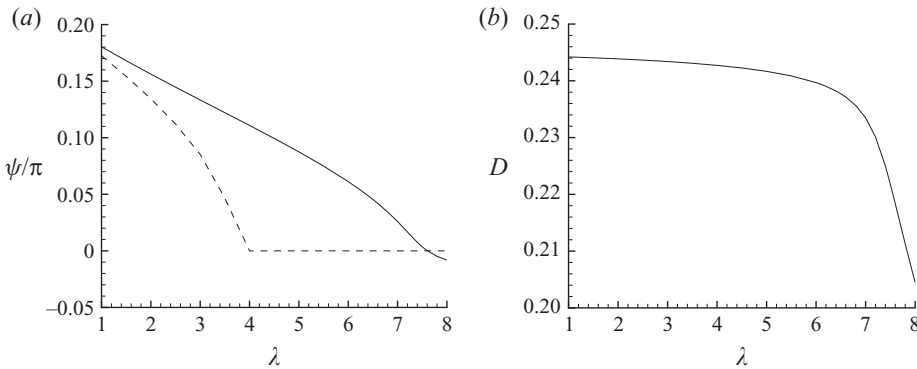

FIGURE 5. The dependence of ψ and D of a $v = 0.95$ vesicle on λ at a fixed shear rate $\chi = 1$. Solid line represents results by DNS, dashed line represents those by leading-order perturbation theory (Misbah 2006).

perturbation analysis predicts ψ to be independent of χ, while a higher-order theory shows that ψ slightly decreases at a higher shear rate (Kaoui *et al.* 2009). In figure 4, we show the dependence of ψ and D on the shear rate at several viscosity ratios from our DNS. The stretching of the vesicle increases slightly at a higher shear rate, causing the small growth of D. The ψ angle also decreases slightly and eventually plateaus as the shear rate increases. Comparing the D-χ curves at different λ values, we note that the deformation factor D appears largely unaffected by λ despite the significant reduction of ψ at higher λ. These are in qualitative agreement with perturbation theories.

We compute the dependence of ψ and D on λ at $v = 0.95$ and fixed shear rate $\chi = 1$, and these are shown in figure 5. The ψ angle decreases monotonically with λ, dropping to below zero at $\lambda > 7.6$. However, since the critical λ value is about 8.46 (by the stability analysis that we discuss later), the TT motion is still stable in spite of the negative inclination angle. In comparison, the ψ calculated by (3.6) becomes zero at a much smaller value $\lambda = 4$, meaning an almost 50 % underprediction of λ_c by the theory. The parameter D sees insignificant change at $\lambda < 7$ so that the change to the shape is similar to a rigid body rotation that aligns the major axis towards the x-direction. When λ further increases from 7 to 8, the semi-axial length in the y- and z-directions almost switches (from 0.86 to 0.81 in y, and from 0.81 to 0.86 in z), while the axial length in x remains almost unchanged at 1.30.
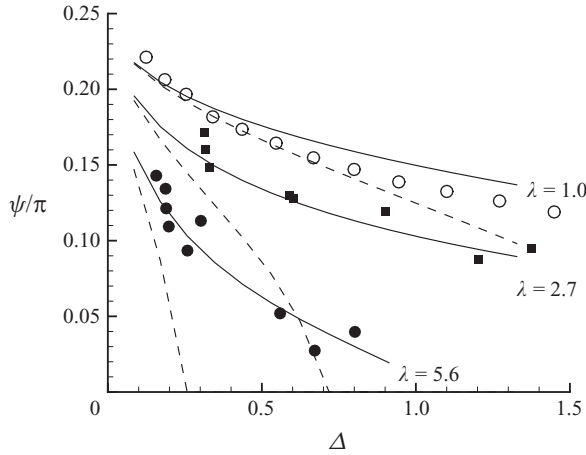
FIGURE 6. The dependence of inclination angles on the excess area of TT vesicles at $\lambda = 1$, 2.7 and 5.6. The TT shape is insensitive to χ at a high shear rate and $\chi = 8$ is chosen for simulation. The solid lines are by our simulation, the symbols represent the measurements at a high shear rate (Kantsler & Steinberg 2005) and the dashed lines are by (3.6) from leading-order perturbation theory (Misbah 2006).

The parameter v (or equivalently Δ), which characterizes the non-sphericity of the vesicle, has significant influence on ψ. In general, the aspect ratio of a vesicle's shape in the shear plane increases with its non-sphericity, and the flow alignment is in turn enhanced resulting in smaller ψ. This trend is also clear by the analytical expression (3.6). The ψ values are calculated as a function of Δ from our DNS at $\lambda = 1$, 2.7 and 5.6, and are shown in figure 6 to be in good agreement with the measurements by Kantsler and Steinberg (Kantsler & Steinberg 2005). The values computed using (3.6) are also plotted; however, quantitative agreement between the theory and DNS occurs only at $\lambda = 1$ and $\Delta < 0.5$, and the theory predicts a much sharper decrease of ψ with increasing Δ at $\lambda = 2.7$ and 5.6.

3.2. *Tank-treading stability*

It is almost trivial to perform the linear stability analysis of the steady-state TT solution once it is obtained, as the Jacobian matrix $\boldsymbol{M} = \partial \dot{\boldsymbol{a}} / \partial \boldsymbol{a}$ is already computed during the Newton iteration. We note that any admissible shape perturbation preserves the total surface area and volume, i.e. the perturbation lies in a linear subspace orthogonal to $\partial A / \partial \boldsymbol{a}$ and $\partial V / \partial \boldsymbol{a}$. From these two vectors, we construct the orthogonal vector pair $\boldsymbol{z}_{1,2}$ using the standard Gram–Schmidt process and define a projection matrix $\boldsymbol{Q}$ to be

$$\boldsymbol{Q} = \boldsymbol{I} - \boldsymbol{z}_1 \otimes \boldsymbol{z}_1 - \boldsymbol{z}_2 \otimes \boldsymbol{z}_2. \tag{3.7}$$

The two non-admissible modes $\boldsymbol{z}_{1,2}$ now are in the null space of the modified matrix $\boldsymbol{Q}^{\mathrm{T}} \boldsymbol{M} \boldsymbol{Q}$ and can easily be excluded. The temporal growth (or decay) factor of each admissible perturbation mode is $\mathrm{e}^{-\mathrm{i}\omega t}$, where $(-\mathrm{i}\omega)$ is an eigenvalue of $\boldsymbol{Q}^{\mathrm{T}} \boldsymbol{M} \boldsymbol{Q}$.

The perturbation mode with $\omega_I > 0$ is unstable, and if $\omega_I < 0$ it is stable. By limiting r as well as its perturbations to the functional form (3.1), we are only considering perturbations symmetric to both the origin and x–z plane. Expanding the permissible perturbation modes to the more general form as dictated in (2.1), we have confirmed that the symmetric perturbation modes are indeed the most unstable ones for TT.

N	$v = 0.95$		$v = 0.90$	
	ω_R	ω_I	ω_R	ω_I
2	4.989	7.336×10^{-2}	5.733	4.172×10^{-1}
4	3.226	-5.602×10^{-2}	3.481	5.782×10^{-2}
6	2.967	-7.542×10^{-2}	2.778	-3.246×10^{-2}
8	2.939	-8.064×10^{-2}	2.618	-6.045×10^{-2}
10	2.937	-8.254×10^{-2}	2.594	-7.647×10^{-2}
12	2.937	-8.295×10^{-2}	2.594	-8.319×10^{-2}
14	2.937	-8.310×10^{-2}	2.592	-8.528×10^{-2}

TABLE 1. The temporal oscillation frequency (ω_R) and growth rate (ω_I) of the most unstable eigenmode for the two TT vesicles shown in figures 2 and 3.

Table 1 lists ω values of the most unstable modes of the two TT solutions shown in figures 2 and 3. The lowest order $N = 2$ expansion incorrectly predicts the steady state to be unstable ($\omega_I > 0$). Thus, an $N = 2$ shape expansion, as used in most perturbation analysis, would underpredict λ_c (Misbah 2006; Danker et al. 2007; Lebedev et al. 2007; Noguchi & Gompper 2007; Vlahovska & Gracia 2007; Messlinger et al. 2009). For $v = 0.95$, the damping rate ω_I obtained with $N = 8$ is within 3 % of that at $N = 14$. For the more non-spherical shape at $v = 0.9$, the convergence is slower as expected, but even the $N = 10$ expansion gives a reasonably accurate ω_I value with a 10 % error when compared to $N = 14$. The oscillating frequency ω_R is also calculated and appears to converge more quickly.

Linear stability calculations are performed to identify the stability boundaries between TT and TR/TU in the $\chi - \lambda$ plane for $v = 0.98$, 0.95, 0.90 and 0.85, which cover the range of Δ from 0.17 to 1.44. All results are plotted in a rescaled two-dimensional phase plane in figure 13, and here we show the neutral curves at $v = 0.95$ and 0.90 calculated from an $N = 8$ expansion in figure 7. We repeat the calculation using a lower order expansion of $N = 4$, and the change to the neutral curve for $v = 0.95$ is insignificant. At $v = 0.90$, the λ_c values are underpredicted by 10 % using $N = 4$, which is expected as the shape demands more spherical harmonic modes to resolve. These neutral curves compare well with the perturbation analysis using a fourth-degree harmonic expansion (Farutin et al. 2010). We do note that the two methods, both using an $N = 4$ expansion, do not generate identical results. The discrepancy is most likely due to the following reasons.

(i) The shape expansion here is only truncated in wavenumber space. For perturbation theory, each spherical harmonic coefficient is further approximated by an asymptotic polynomial expansion of a small parameter such as Δ.

(ii) While the spherical harmonic expansion of r is truncated at $N = 4$, the surface forces are fully resolved on the 32×64 mesh, whereas in perturbation theory they are filtered in a manner similar to r.

The perturbation theories predict that the bifurcation is of saddle point type at a low shear rate and of Hopf type at a high shear rate. In figure 7, the change of the bifurcation type is indicated by the discontinuity in the slope of the neutral curve that occurs near $\chi = 0.25$ for $v = 0.95$ and $\chi = 0.6$ for $v = 0.9$. The bifurcation can be identified by the dependence of the most unstable ω on λ as $\lambda \to \lambda_c$. For example, figure 8 shows that ω at a low shear rate $\chi = 0.2$ is purely imaginary near the bifurcation and demonstrates a square root dependence as typical of a saddle
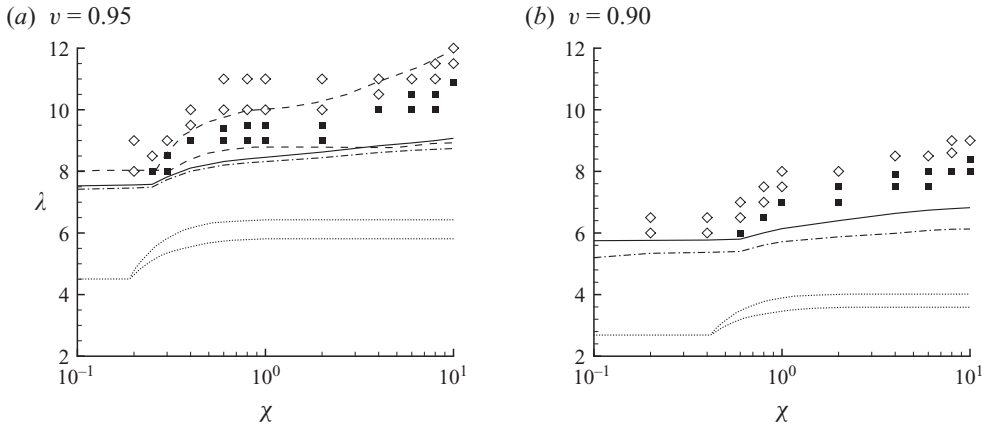
(a) $v = 0.95$

(b) $v = 0.90$

FIGURE 7. Phase diagram of transition between in-plane TT, TR and TU. Critical λ values for TT are obtained by (········) perturbation theory using second-degree harmonic expansion for the surface shape (Lebedev *et al.* 2007); (– – – –) perturbation theory using fourth-degree harmonic expansion (Farutin *et al.* 2010); (———) current linear stability calculation using eighth-degree expansion; (—·—) current linear stability calculation with fourth-degree expansion. ■ denotes TR motion and ◇ TU by DNS. A recent DNS also reports good agreement with the theory using fourth-degree expansion (Biben *et al.* 2009).
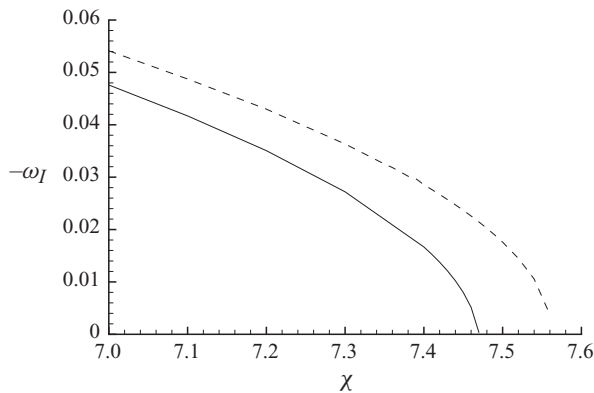
FIGURE 8. The most unstable ω as $\lambda \to \lambda_c$ at $\chi = 0.2$ and $v = 0.95$. Solid line is by fourth-degree shape expansion and dashed line is by eighth degree expansion.

point bifurcation. Because of the rapid diminution of ω_I as $\lambda \to \lambda_c$, the λ_c predicted by $N = 4$ and 8 are close in value even though the relative error in ω_I itself becomes quite large.

For the Hopf bifurcation, the most unstable mode has complex ω; therefore, at a value of λ that is below but close to λ_c, we expect the vesicle shape to oscillate while converging to the final steady TT state. This is demonstrated by the oscillatory decay of the inclination angle ψ at $\chi = 10$ in figure 9. From the ψ–t curve, the value of the most unstable ω is extracted to be $(2.94, -0.805)$, which is in good agreement with $\omega = (2.94, -0.810)$ by the linear stability analysis.

The shape of the most unstable modes near the stability boundaries is calculated at low shear ($\chi = 0.2$) and high shear ($\chi = 8$), and are shown in figure 10. At the low shear, ω is pure imaginary, and the eigenmode represents a rigid-body tilt in the shear plane. At the high shear, the pair of eigenvalues are complex conjugate, and the two
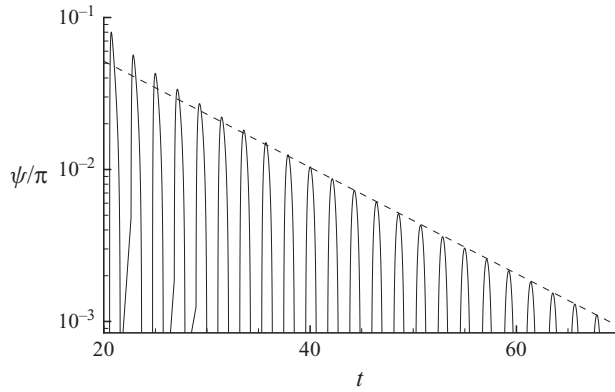
FIGURE 9. The inclination angle of a vesicle as it relaxes to the steady TT state. $v = 0.95$, $\lambda = 8.0$ and $\chi = 10.0$.
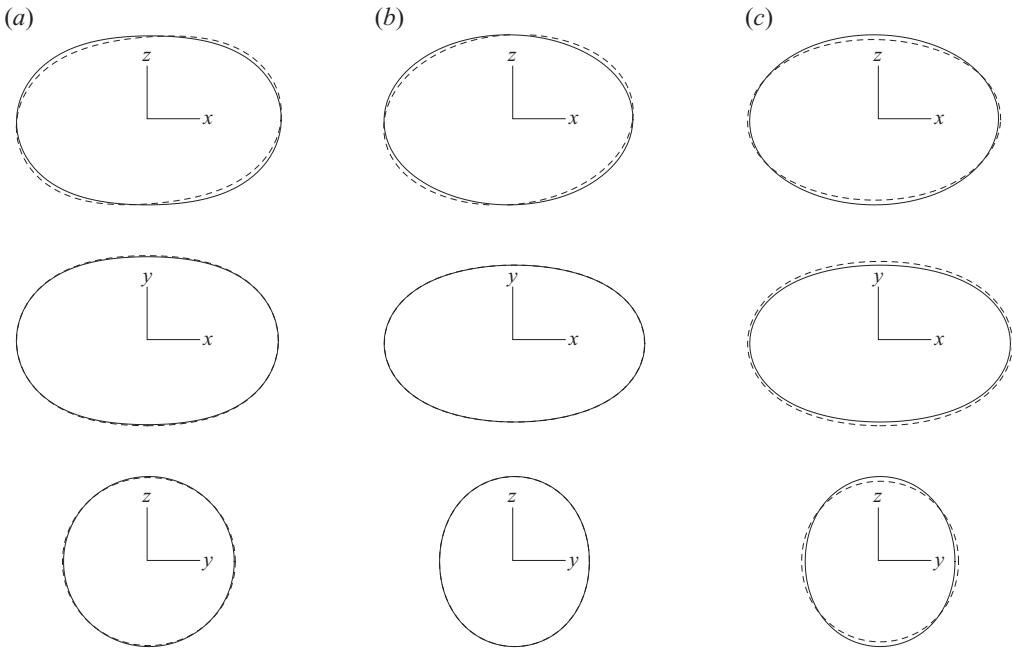

FIGURE 10. The most unstable mode of steady-state TT solutions. The solid lines are the contours of the base state, and the dashed lines with the eigenmode superimposed. (a) Low shear ($\chi = 0.2$, $\lambda = 7.5$). (b, c) Higher shear ($\chi = 8$, $\lambda = 9$), and the real and imaginary parts of the eigenmodes are plotted separately.

modes from the real and imaginary parts of the eigenvector pair are distinct: one is tilting similar to that at low shear, and the other represents a 'breathing' motion, i.e. the expansion and contraction along the axial directions. These eigenmodes clearly resemble the motion patterns in the TU and TR regimes.

3.3. Trembling and tumbling

At $\lambda > \lambda_c$, the transition to TU happens either immediately at low shear, or gradually with increasing λ through an intermediate TR motion at high shear. Figure 11 shows the time variation of inclination angle during TR and TU motion cycles. For TR, ψ
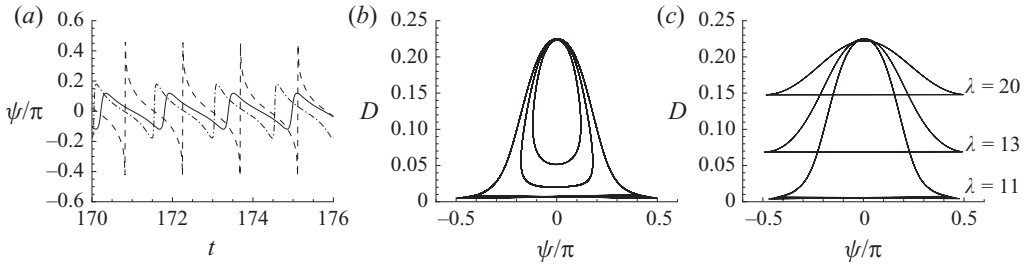
FIGURE 11. A $v = 0.95$ vesicle's inclination and deformation in TR and TU regimes at the same shear rate $\chi = 8$. (a) Time variation of ψ at $\lambda = 10$ (———), $\lambda = 10.5$ (—·—) and $\lambda = 11$ (– – – –). (b) The orbits in the D–ψ plane during the TR to TU transition. The orbital curve expands as λ increases from 10 to 10.5 and eventually 11. (c) The orbits in the TU regime.
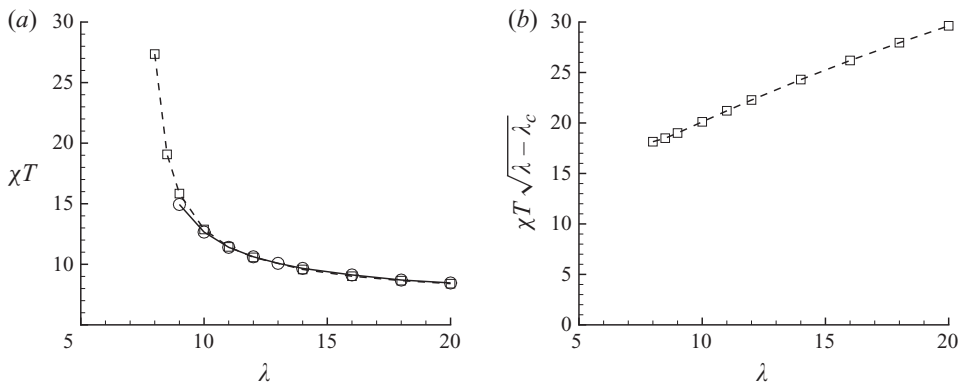

FIGURE 12. (a) The time period of TR and TU at $\chi = 0.2$ ($\square$) and at $\chi = 6$ ($\bigcirc$). (b) Rescaled time period at $\chi = 0.2$.

oscillates with a magnitude smaller than $\pi/2$, and is a smooth function of time. As λ increases, the oscillation amplitude increases, and the transition between ψ minimum and maximum happens more rapidly until ψ becomes discontinuous, at which point the vesicle starts to tumble. Of course, the shape of a TU vesicle still varies smoothly with time, and the periodic jump of ψ from $-\pi/2$ to $\pi/2$ merely means that the vesicle's major axis passes through the z-axis.

The orbits of the motion are plotted in the ψ–D plane in figure 11, which demonstrates the significant shape variation of the vesicle during each motion cycle. The difference between L_1 and L_2 (i.e. in-plane stretching) is maximal when the long axis is parallel to the x-direction, and is minimal when the long axis is along the z-direction in TU or during the rapid axis-swapping in TR. The variation in both ψ and D of the orbits in the TR regime increases with λ, and the orbit eventually evolves into a bell-shaped one when TU happens. The strongest variation of D appears to occur at the TR/TU boundary, and then decreases with increasing λ in the TU regime when the vesicle resembles a rigid particle.

Figure 12 shows the normalized TR and TU time period χT, where T is defined as the time interval between two consecutive minima in ψ. For the low shear $\chi = 0.2$ case, the vesicle undergoes the direct TT-to-TU transition at $\lambda_c = 7.56$, at which point the most unstable mode has zero temporal growth rate and is non-oscillatory. The TU time period appears to be singular as $\lambda \to \lambda_c^+$, and the rescaled plot (the right of figure 12) shows that $T \propto (\lambda - \lambda_c)^{-1/2}$ near the transition, as predicted by the

perturbation theory (Vlahovska & Gracia 2007) even though the theory underpredicts the actual λ_c by 50 %. At the higher shear rate $\chi = 6$, the TT-to-TR transition occurs first at $\lambda_c = 8.92$, where the most unstable mode is oscillatory with temporal frequency $\omega_R = 2.48$. This corresponds to a characteristic time period $T = 2\pi/\omega_R = 2.53$, which is close to the TR time period $T = 2.49$ at $\lambda = 9$ by DNS.

The two χT versus λ curves at $\chi = 0.2$ and 6 almost collapse in the overlapping λ range, indicating that χT is shear rate insensitive, also in agreement with perturbation theory (Kaoui *et al.* 2009). We have not observed a noticeable singularity in T at the TR-to-TU transition near $\lambda = 10.7$ at $\chi = 6$.

The maximum λ value studied here is 20, and figure 11 shows that there is still significant variation in D and thus axial length in time. At $\lambda = 20$, the TU period is $\chi T \approx 8.4$, while an ellipsoid with the same axial lengths as that of the vesicle at the TT/TB transition (where $D = 0.22$) has a half rotation period 6.97 (note that one rigid body rotation is analogous to two TUs). Truly rigid-body rotations can only be realized at even higher λ values.

The in-plane orbit at $\lambda = 20$ appears to be stable: the two axes in the x–z plane do not tilt away from the shear plane after 50–100 TUs in our DNS at both low and high shear rates ($\chi = 0.2$ and 8, respectively). A 'kayaking' motion at $\lambda = 20$ is reported elsewhere (Biben *et al.* 2009), but no clear details are provided. In the last section of this manuscript, we demonstrate that off-the-shear-plane motions do exist, but an initial tilted configuration is necessary because the in-plane TR and TU orbits are stable to small tilting perturbations.

3.4. *Phase diagram*

According to leading-order perturbation analysis (Lebedev *et al.* 2007), the dynamics of a vesicle in shear is completely characterized by the two parameters

$$S = \frac{7\pi}{3\sqrt{3}} \frac{\chi v}{\Delta} \qquad \Lambda = \frac{4}{\sqrt{30\pi}} \sqrt{\Delta} \left(1 + \frac{23}{32}\lambda\right), \tag{3.8}$$

and the boundaries between TT/TR/TU collapse in the same S–Λ plane, as plotted by the dashed curve in figure 13. Note that the extra v factor in S is due to the fact that the capillary number χ is defined using the radius based on a vesicle's volume by Lebedev *et al.* (2007), while it is based on the surface area here. From the definition of Λ, it is clear that λ_c decreases with increasing Δ, which is in agreement with our linear stability analysis at $v = 0.95$ and 0.9. In figure 13, the transition boundaries at $v = 0.98$, 0.95, 0.9, and 0.85 obtained by our DNS are plotted in the same S–Λ plane; the excess area Δ of these calculations ranges between 0.17 at $v = 0.98$ and 1.44 at $v = 0.85$. The difference between the theory and DNS is obvious: DNS consistently predicts higher λ_c values and wider width in Λ for the TR regime. The discrepancy between the DNS and the perturbation theory increases with Δ, which is not unexpected.

Perturbation theories that expand the deformation in higher-order polynomials of Δ while retaining the same second-degree harmonic expansion do not introduce significant change to the underpredicted λ_c values (Danker *et al.* 2007). Therefore, shape expansion using fourth-degree harmonics is necessary for quantitative perturbation analysis even at very moderate Δ values.

3.5. *Particle stress*

In a dilute vesicle suspension, the contribution from vesicles to the mean stress tensor $\langle \boldsymbol{\sigma} \rangle$ is defined to be $\boldsymbol{\sigma}^p$ so that

$$\langle \sigma_{ij} \rangle = -\langle p \rangle \delta_{ij} + 2\mu \langle e_{ij} \rangle + \sigma_{ij}^p. \tag{3.9}$$

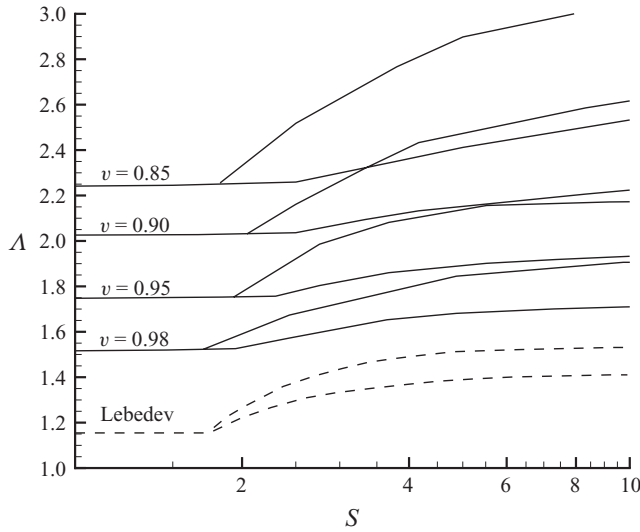FIGURE 13. The flow bifurcations obtained by DNS (———) and by theory (– – – –) (Lebedev *et al.* 2007).

The $\boldsymbol{\sigma}^P$ due to any single vesicle can be calculated by the boundary integral formulation (Batchelor 1970; Pozrikidis 2003)

$$\sigma_{ij}^P = \frac{1}{\Omega} \int_D [\![f_i]\!] \, x_j \, \mathrm{d}A + \frac{1}{\Omega} \int_D (\lambda - 1)\mu(u_i n_j + u_j n_i) \, \mathrm{d}A, \qquad (3.10)$$

where Ω is the volume of the whole system. If there are now N non-interacting vesicles in the volume Ω, then the particle contribution to the stress is $N\boldsymbol{\sigma}^P$. To specify the particle stress in such a suspension, we first note that upon reversal of the flow direction (i.e. when $\dot{\gamma}$ changes sign), the steady-state shear stress component σ_{xz}^P changes sign while the normal components do not. We therefore define the components of the non-dimensional particle specific stress tensor $\boldsymbol{S}$ to be

$$S_{xz} = \sigma_{xz}^P/(c\mu\dot{\gamma}) \qquad (3.11)$$
$$N_1 = S_{xx} - S_{zz} = (\sigma_{xx}^P - \sigma_{zz}^P)/(c\mu|\dot{\gamma}|) \qquad (3.12)$$
$$N_2 = S_{zz} - S_{yy} = (\sigma_{zz}^P - \sigma_{yy}^P)/(c\mu|\dot{\gamma}|), \qquad (3.13)$$

where $c = V/\Omega$ is the vesicle volume fraction. The normal components of $\boldsymbol{\sigma}^P$ are scaled by $\dot{\gamma}$ instead of $\dot{\gamma}^2$ (the latter being commonly used for liquid drops) because the vesicle's deformation is only weakly dependent on the shear rate. Take a TT vesicle for example, since its reduced volume must remain constant, the vesicle cannot be stretched indefinitely by the flow. Indeed, the shape becomes insensitive to $\dot{\gamma}$ at high shear, and the surface force distribution is dominated by the surface tension force that as a constraint force scales with $\dot{\gamma}$. Therefore, the linear scaling of $\boldsymbol{\sigma}^P$ with $\dot{\gamma}$ should be expected at least at a high shear rate. The scalings are further confirmed in our numerical results by the collapse of $\boldsymbol{S}$ curves at very different shear rates. In this section, we describe the rheological features observed from our DNS. Discussion of the underlying mechanism, as well as the comparison with theories and other simulation results, are deferred to the next section.
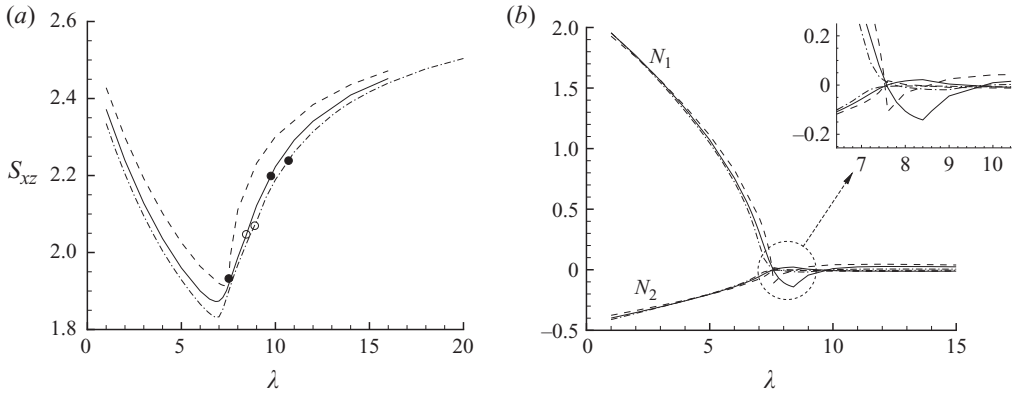
FIGURE 14. Components of the vesicle specific relative viscosity tensor as a function of viscosity ratio λ at $\chi = 0.2$ (– – – –), $\chi = 1.0$ (———) and $\chi = 6.0$ (— · —). $\circ$ marks the transition to TR and $\bullet$ to TU. $v = 0.95$.

Figure 14 shows S_{xz} and $N_{1,2}$ as functions of λ at $\chi = 0.2$, 1 and 6. In the TT regime, $\boldsymbol{S}$ is constant in time; for TR and TU motions, the time averages of $\boldsymbol{S}$ are used. The most prominent feature of S_{xz} is its non-monotonic dependence on λ. At low shear ($\chi = 0.2$), the minimum S_{xz} occurs at the TT-to-TU transition, where a cusp singularity is exhibited similar to that predicted by the leading-order perturbation theory (Danker & Misbah 2007). At high shear, S_{xz} reaches its minimum within the TT regime at $\lambda < \lambda_c$ before the TT-to-TR transition. The cusp singularity of S_{xz} no longer exists, and there is no discontinuity in the slope of S_{xz} as a function of λ. The behaviour at high shear by DNS is thus qualitatively different from the prediction by the leading-order theory but is in agreement with a high-order perturbation theory that expands the shape to high powers of Δ (Danker *et al.* 2007).

Figure 14 also shows that the $N_{1,2}$ components decrease in the TT regime as λ increases and approach zero from opposite directions. Both N_1 and N_2 vanish in the TR and TU regimes. These features qualitatively agree with perturbation theories, but the quantitative difference is significant: the theory predicts that $N_2 = -N_1/2$ (Danker & Misbah 2007; Vlahovska & Gracia 2007), while the ratio N_1/N_2 in TT is close to -5 by our DNS.

As shown in figure 15, S_{xz} in the TR regime is time periodic and has a local minimum in every motion cycle when the inclination angle ψ undergoes the rapid transition from its negative minimum to positive maximum. Similarly for tumbling vesicles, a local minimum of S_{xz} occurs when the major axis is aligned with the z-axis. The global minimum of S_{xz} happens when the major axis aligns with the x-axis. The minima of the shear viscosity at $\psi = 0$ and $\pi/2$ are also predicted by perturbation theories and two-dimensional DNS (Danker & Misbah 2007; Ghigliotti *et al.* 2010), where however S_{xz} at the two minima have the same value. The differences are explained in the next section.

The plot of S_{xz} versus χ in figure 16 shows that vesicle suspension is shear thinning and the thinning exponent is higher at a low shear rate. The motion is in the TT regime throughout the range of χ at $\lambda = 1$, 2 and 4, and undergoes the TB-to-TR-to-TT transition with increasing χ at $\lambda = 8.7$. Overall, the shear thinning is quite weak as the reduction of S_{xz} is only about 10 % when χ increases from 0.2 to 10 for all four λ values studied.
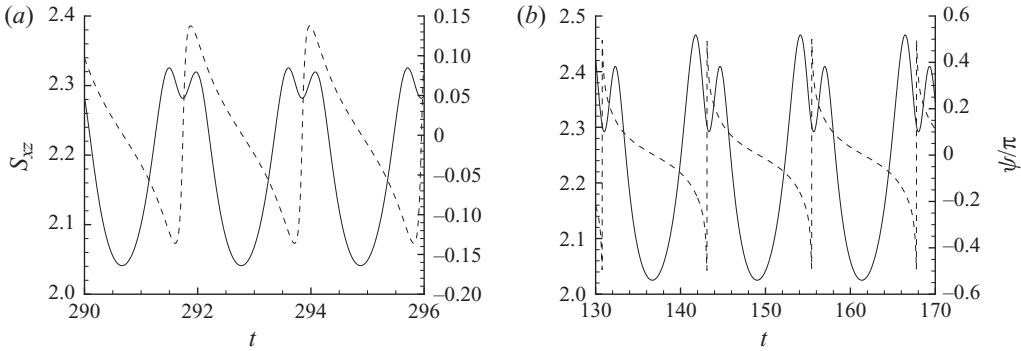
FIGURE 15. Time variation of S_{xz} (——) and inclination angle ψ (----) of (a) TR vesicle with $v = 0.95$, $\lambda = 10$ and $\chi = 6$; (b) tumbling vesicle with $v = 0.95$, $\lambda = 10$ and $\chi = 1$.
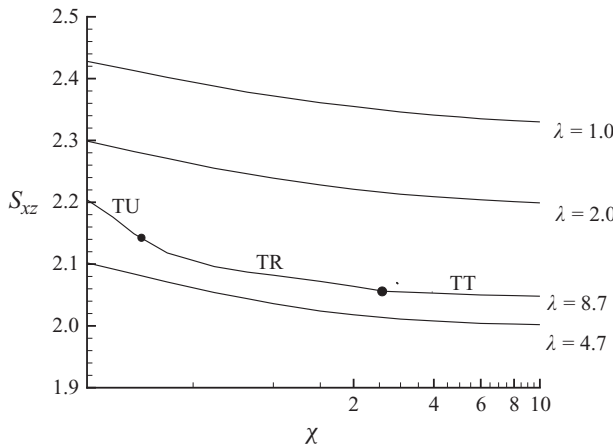

FIGURE 16. Intrinsic shear viscosity versus shear rate. $v = 0.95$.

3.6. Analysis of the S_{xz} and N_1 components

By leading-order theory (Danker & Misbah 2007), the instantaneous particle stress is

$$S_{xz} = \frac{5}{2} - \sqrt{\frac{30}{\pi}} h + \frac{h}{\Delta} \sqrt{\frac{480}{\pi}} R^2 \sin^2(2\psi) \tag{3.14}$$

$$N_1 = -2N_2 = \frac{h}{\Delta} \sqrt{\frac{480}{\pi}} R^2 \sin(4\psi), \tag{3.15}$$

where $h = 60\sqrt{2\pi/15}/(23\lambda + 32)$, ψ is the inclination angle and R is the 'amplitude of the deformation about the sphere'. At TT, $R = \sqrt{\Delta}/2$ and

$$S_{xz} = \frac{5}{2} - \sqrt{\frac{15}{8\pi} \frac{\Delta}{h}} \tag{3.16}$$

$$N_1 = -2N_2 = \sqrt{\frac{15\Delta(4h^2 - \Delta)}{2\pi h^2}}. \tag{3.17}$$

Therefore, as λ increases, h decreases and so S_{xz} and N_1 decrease —— equivalent to the trend in the DNS. Because ψ predicted by theory diminishes much faster with increasing λ than calculated by our DNS, there is no quantitative agreement between the two. An important aspect of (3.17) is the absence of χ so that both S_{xz} and $N_{1,2}$ are
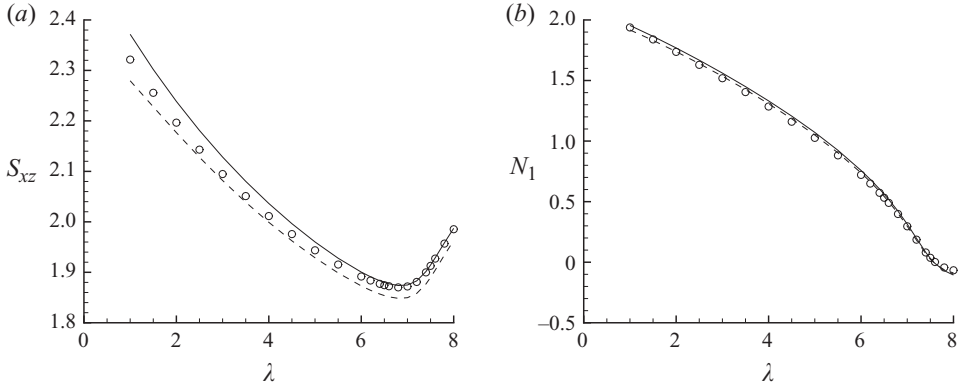
FIGURE 17. The components of particle specific stress: (———) the full component; (– – – –) the portion due to flow resistance (i.e. with contribution from bending force neglected); (◯) ellipsoid approximation (also without bending).

shear rate independent. This mirrors the weak χ-dependence of our DNS results, and suggests that the contribution from the surface bending force to $\boldsymbol{S}$ is small (see below).

By (2.14), the velocity field and the surface tension force $\boldsymbol{f_\sigma}$ can both be considered as the sum of two parts that are driven by (i) $-N\boldsymbol{f_B}/(8\pi\mu)$ and (ii) $\boldsymbol{u}^\infty$ respectively. Therefore, the instantaneous particle stress tensor has decomposition $\boldsymbol{S} = \boldsymbol{S}^B + \boldsymbol{S}^V$, where the superscript 'B' denotes a bending force contribution and 'V' is due to the resistance to the background shear flow. Two separate computations are needed to compute $\boldsymbol{S}^B$ and $\boldsymbol{S}^V$, with the right-hand side of (2.14) replaced by $-N\boldsymbol{f_B}/(8\pi\mu)$ and $\boldsymbol{u}^\infty$, respectively. For a given vesicle's shape and orientation, $\boldsymbol{\sigma}^B$ is a linear functional of $\boldsymbol{f_B}$ and is independent of χ, and hence $\boldsymbol{S}^B \propto \chi^{-1}$. On the other hand, $\boldsymbol{\sigma}^V$ is linear about $\boldsymbol{u}^\infty$, and so $\boldsymbol{S}^V$ is independent of χ.

We now apply the particle stress decomposition to the TT solution at $v = 0.95$ and at a moderate shear rate $\chi = 1$. Figure 17 shows that $\boldsymbol{S}^V$ is the dominant contributor to S_{xz} and N_1; however, N_2^B is comparable to N_2^V (not shown here). In addition, the S_{xz}^V and N_1^V of vesicles of strictly ellipsoidal shapes with the same orientation and axial lengths closely approximate those of the vesicle.

The effect of inclination angle, viscosity contrast and axial lengths is investigated by computing S_{xz}^V and N_1^V of an equivalent ellipsoid. First, we fix the axial lengths to be those of the vesicle at $\lambda = 7$. The resulting contour plots of S_{xz} and N_1 in the $\psi-\lambda$ plane are shown in figure 18. These contours exhibit high symmetries about ψ because of the linearity of the Stokes flow governing equation, the symmetry in $\boldsymbol{u}^\infty$ and the ellipsoidal shape. In table 2, we list the symmetry of $\boldsymbol{S}^V$ upon mirroring the ellipsoid about the $x-y$ plane ($\psi \to -\psi$, i.e. $(x, y, z) \to (x, y, -z)$), in simple shear flow and in pure straining flow.

The strain part of $\boldsymbol{u}^\infty$, with principle axes along the $\psi = \pm\pi/4$ direction, is what primarily contributes to S^V. In the reference frame of axes $\boldsymbol{e}'_x = (\boldsymbol{e}_x + \boldsymbol{e}_z)/\sqrt{2}$, $\boldsymbol{e}'_y = \boldsymbol{e}_y$, $\boldsymbol{e}'_z = (-\boldsymbol{e}_x + \boldsymbol{e}_z)/\sqrt{2}$, the tensor components of interests are

$$S'_{xx} = (S_{xx} + S_{zz})/2 + S_{xz} \tag{3.18}$$
$$S'_{zz} = (S_{xx} + S_{zz})/2 - S_{xz} \tag{3.19}$$
$$S'_{xz} = S_{zz} - S_{xx} \tag{3.20}$$
$$S'_{yy} = S_{yy}, \tag{3.21}$$

	Simple shear	Strain
$\boldsymbol{u}^{\infty}$	$(z, 0, 0)$	$(x, 0, -z)$
$\boldsymbol{S}$	$\begin{pmatrix} - & - & + \\ - & - & + \\ + & + & - \end{pmatrix}$	$\begin{pmatrix} + & + & - \\ + & + & - \\ - & - & + \end{pmatrix}$

TABLE 2. The symmetry of $\boldsymbol{S}^V$ of an ellipsoid upon a mirroring operation ($\psi \to -\psi$). '+' denotes even symmetry and '−' odd symmetry.

	$\psi = 0$	$\psi = \pi/4$
S_{xz}	+	+
$N_1 = S_{xx} - S_{zz}$	−	−
$N_2 = S_{zz} - S_{yy}$	−	none
$N_1/2 + N_2$	−	+

TABLE 3. The symmetry of $\boldsymbol{S}^V$ components about $\psi = 0$ and $\pi/4$ in the simple shear flow.
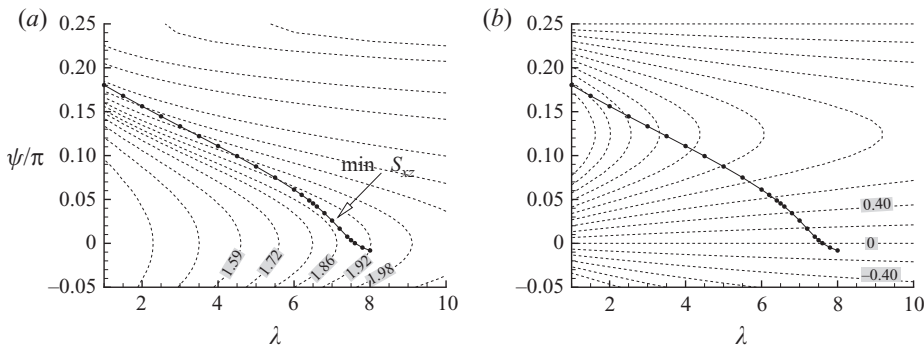

FIGURE 18. The contour plots of S_{xz} (a) and N_1 (b) of an ellipsoid in the λ–ψ plane. The ● symbols denote the trajectory of a TT vesicle in this phase space.

and their symmetries about $\boldsymbol{e}'_x$ (i.e. $\psi = \pi/4$ direction) are those for the strain flow given in table 2. Writing the components of $\boldsymbol{S}$ in terms of those of $\boldsymbol{S}'$, we obtain their symmetries about $\psi = \pi/4$, which are listed in table 3.

This simple analysis results in the same symmetry of S_{xz} and N_1 about $\psi = 0$ and $\pi/4$ as that predicted by (3.15), and the same symmetry is obtained by our DNS of ellipsoids in shear flow, as demonstrated by their contour plots in figure 18. The S_{xz} component is a monotonically increasing function of λ and of ψ for $\psi \in (0, \pi/4)$. For the TT vesicle, the non-monotonic dependence of S_{xz} on λ results from the competing effects of decreasing ψ and increasing λ. At $\lambda < 7$, the decrease in ψ is fast enough so that the vesicle's trajectory in the ψ–λ plane is opposite to the gradient of S_{xz}; beyond $\lambda = 7$, the change in ψ is small, and S_{xz} grows slightly due to the increase of λ.

We repeat the calculation of S_{xz} in the ψ–λ plane, but with axial lengths being those of the vesicle at $\lambda = 8$, so in effect switching the axial length in y–z cross-section. The contour plot remains qualitatively the same, but the quantitative difference is obvious. At $\psi = 0$ and $\lambda = 8$, S_{xz} increases from 1.92 in the previous calculation to 1.98 after
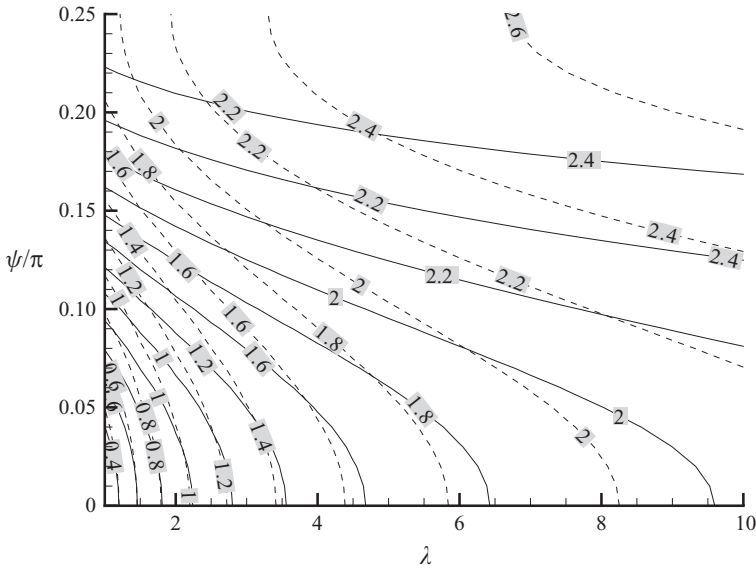
FIGURE 19. The contour plots of S_{xz} of two ellipsoids of $D = 0.233$ (solid contour line) and $D = 0.204$ (dashed line).

the shape change. Therefore, the increase in λ and the change in shape contribute comparably to the increase of S_{xz}. Figure 19 shows that the effect of shape change on S_{xz} is very complicated: the decrease in D makes S_{xz} increase in some regions (including both $\psi = 0$ and $\pi/2$ lines) in the ψ–λ plane but causes it to decrease elsewhere.

Because of the even symmetry of S_{xz} about $\psi = \pi/4$, it has minima at $\psi = 0$ and $\pi/2$. The minima are equal in their values, provided that the shapes at these two orientations are the same. For a vesicle in two dimensions, the lengths of its two axes are largely fixed by its area and perimeter, and numerical simulations show that the S_{xz} values of a tumbling vesicle at $\psi = 0$ and $\pi/2$ are the same (Ghigliotti et al. 2010). In three dimensions, the axial lengths vary in time because of the extra degrees of freedom in the vorticity direction, as demonstrated by the significant variations of D during TR and TU in figure 11. The D is minimal when the vesicle undergoes the major/minor axes swapping during TR or when its major axis passes through the z-axis in tumbling, and so the instantaneous flow resistance is higher than that at $\psi = 0$ with larger D. At very high λ values, the vesicle acts as a rigid particle, so the variation of the axial lengths as well as the resulting difference between S_{xz} minima should diminish.

In contrast to S_{xz}, N_1 has odd symmetry about both $\psi = 0$ and $\pi/4$. At fixed λ, the maximum of N_1 occurs at $\psi = \pi/8$. However, the trajectory of the vesicle in the λ–ψ plane remains opposite to the gradient direction of N_1, resulting in its monotonic decay as the transition to TR is approached. When ψ drops below zero near flow transition, N_1 becomes slightly less than zero due to its odd symmetry about $\psi = 0$. Lastly, since N_1 switches its sign every $\pi/4$ angle, it is therefore not surprising that it has zero time average when the vesicle trembles or tumbles.

We now briefly discuss shear thinning, i.e. the slight decrease of S_{xz} at fixed λ as χ increases, shown in figure 16. We first note that the vesicle's shape is insensitive to χ in the TT regime. The bending force contribution to $\boldsymbol{\sigma}^p$ is thus largely independent
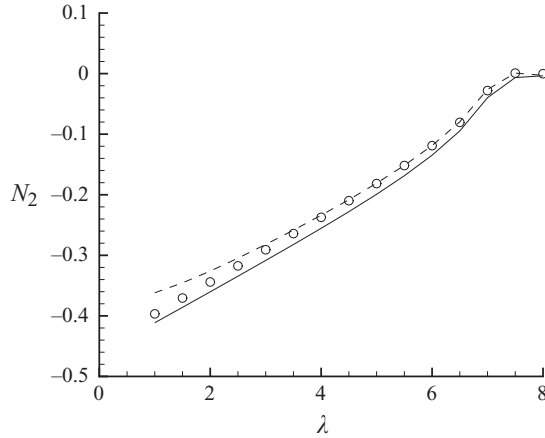
FIGURE 20. The N_2 stress component of a TT vesicle at $\chi = 6$: (———) the full component; (– – – –) N_2^V; ○ N_2^V of the equivalent ellipsoid.
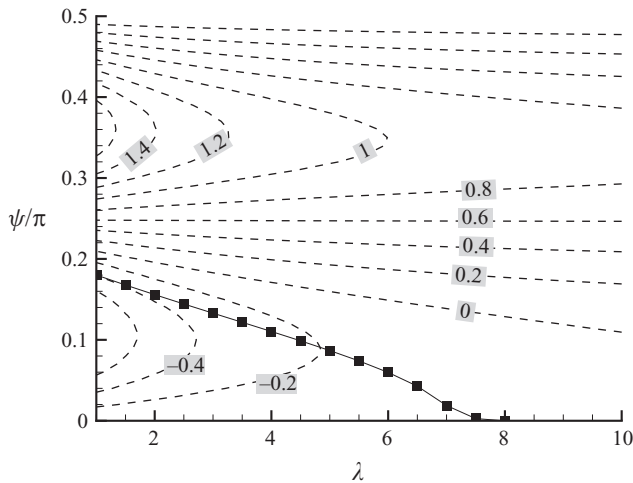

FIGURE 21. The N_2 contour of an ellipsoid in the λ–ψ plane. The solid square symbols denote the trajectory of a TT vesicle at $\chi = 6$ in this phase space.

of $\dot{\gamma}$, and as discussed $S_{xz}^B \approx \chi^{-1}$ is shear thinning. On the other hand, the vesicle is slightly tilted towards the x-direction and is stretched more at higher values of χ: the former reduces S_{xz}, while the latter can either enhance or reduce S_{xz}^V. The overall effect is that S_{xz} decreases by an amount comparable to the decrease in S_{xz}^B.

3.7. *Analysis of N_2*

The contribution to $N_2 = S_{zz} - S_{yy}$ from the bending force remains significant for the whole λ-range at $\chi = 1$; hence, the ellipsoid analogy does not apply for N_2. The N_2^B is reduced by about a factor 5 at a higher shear rate $\chi = 6$ so that N_2^V becomes the dominant part and its magnitude is more than seven times that of N_2^B for $\lambda \leqslant 6$. Figure 20 shows that N_2^V of the vesicle and of the equivalent ellipsoid both approximates the full N_2 component reasonably well at $\chi = 6$.

In figure 21, we show the contour of N_2 of the equivalent ellipsoid with axial lengths being 1.305 and 0.907 in the x–z plane and 0.788 in the y-direction – same as the axial

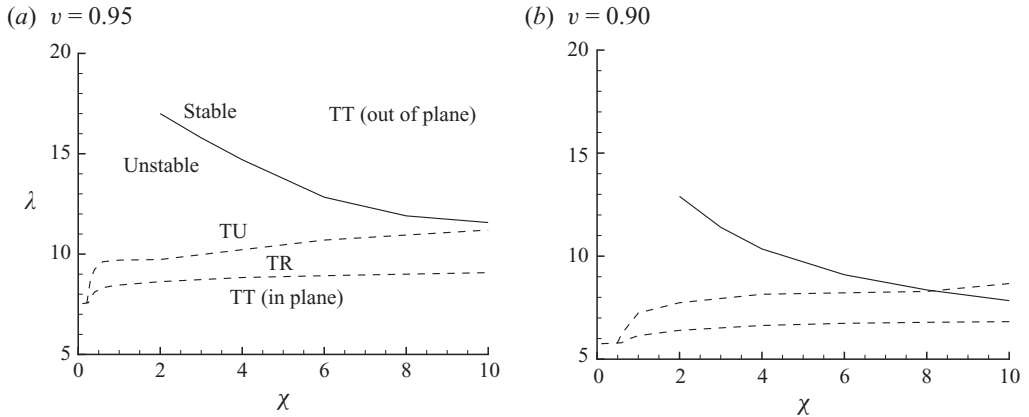(a) $v = 0.95$ (b) $v = 0.90$

FIGURE 22. The stability boundary of the out-of-plane TT motion. Solid line represents the transition boundary. For comparison, dashed line is the sketch of the transition boundaries of the in-plane motion.

lengths of the $v = 0.95$ TT vesicle at $\lambda = 1$ and $\chi = 6$. As discussed in the previous section, N_2 does not have either even or odd symmetry about $\psi = \pi/4$. However, the contour lines of N_1 and N_2 follow the same trend, and the ratio $N_1/N_2 \approx -5$ along the trajectory of the vesicle in the λ–ψ plane. This ratio is very different from the value -2 as predicted by (3.15).

Our discussion of the physical mechanisms regarding N_2 here is limited to the high shear rate $\chi = 6$. This does not explain why the N_2 curves at $\chi = 0.2$, 1 and 6 all collapse in figure 14. Further investigation is necessary, and perturbation analysis, especially using high-degree harmonic expansion, should be extremely useful in providing insights into the behaviour of these second normal stresses.

3.8. *Out-of-plane orbits*

The shape of a vesicle, either TT, TR or TU, is symmetric about the x–z plane, within which its major axis lies. The so-called spinning motion was first reported by using perturbation analysis (Lebedev, Turisyn & Vergeles 2008). A spinning vesicle's long axis rotates about the vorticity direction, but unlike in-plane tumbling, the angle between the axis and flow vorticity is not equal to $\pi/2$ and so the shape is not symmetric about the x–z plane. Using our DNS, we investigate general three-dimensional out-of-plane motions, as discussed below.

First, we have identified an alternative TT motion where the major axis is aligned with flow vorticity. Stability analysis shows that the critical λ value is significantly higher than the λ_c for in-plane TT at the same shear rate. The motion is stable when $\lambda > \lambda_c$, while a Hopf bifurcation occurs when λ drops below λ_c. At this point, while the TT motion remains stable to perturbations symmetric about the x–z plane, it becomes unstable to non-symmetric perturbations. It is thus necessary to include perturbation modes of $\bar{P}_{lm}(\cos\theta)\sin m\phi$ with even l.

Figure 22 shows the stability boundaries at $v = 0.95$ and 0.9, and these are compared with the diagram of the in-plane motion. At high shear, the stable out-of-plane TT regime overlaps with the in-plane TR and TU regimes, and its λ_c increases rapidly with decreasing χ. The magnitude of the most unstable ω_I however remains small in the unstable regime even when λ is far below λ_c. For example, at $v = 0.95$ and $\chi = 4$, $\lambda_c = 14.7$, while at $\lambda = 11$, the most unstable mode has $\omega_I = 5.56 \times 10^{-3}$. The bifurcation
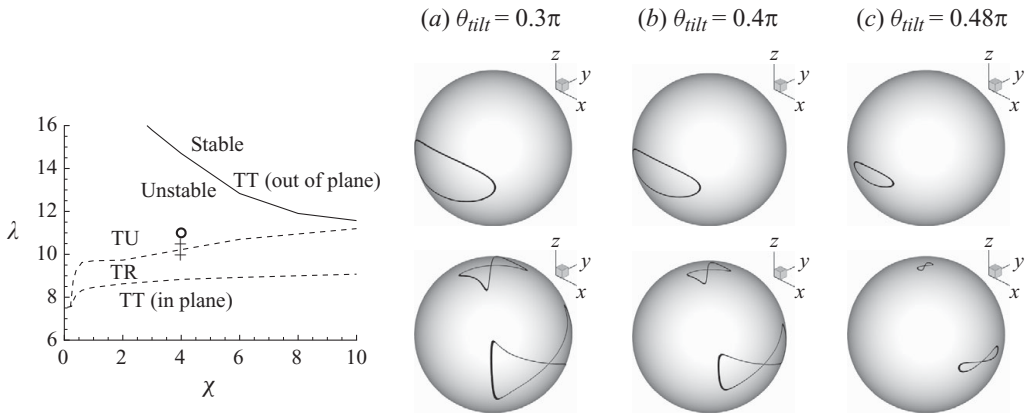
FIGURE 23. Periodic rotation of the principle axes of a vesicle initially tilted from the x–z plane by an angle θ_{tilt}. The vesicle has $v = 0.95$, $\lambda = 11$ and $\chi = 4$, as labelled by '$\bigcirc$' in the phase diagram on the left. On top are the trajectories of the major axis projecting on the unit sphere, and on bottom the two minor axes.

is of Hopf type in the range of χ studied. Considering the small magnitudes of ω_I near bifurcation, one would expect the persistence of out-of-plane TRs at $\lambda < \lambda_c$.

We use DNS to further explore general three-dimensional out-of-plane motions. The so-called 'kayaking' motions are reported at very high internal viscosity $\lambda = 20$ (Biben *et al.* 2009), where the vesicle's motion is expected to approximately follow the Jeffery's orbit. The regime in the χ–λ plane explored here is different with λ slightly above the TR-to-TU transition and well below the neutral curve of the out-of-plane TT, as marked by the symbols in figure 23. At these moderate λ values, the axial length undergoes large variations in time, much like the in-plane TR and TU. To create a tilted vesicle as initial condition, an instantaneous vesicle shape symmetric about the x–z plane is rotated by an angle θ_{tilt} about its shorter axis in the x–z plane. After some initial transition, the vesicle shape eventually follows a periodic orbit in all our simulations. The trajectories of a vesicle's three orientation vectors are plotted in figure 23, where the vesicle is tilted by several different angles initially. For the small initial perturbation $\theta_{tilt} = 0.2\pi$, the vesicle reverts to the in-plane tumbling motion (not shown here). Out-of-plane motions occur at larger initial θ_{tilt} angles. The orbit of the major axis is similar to a Jeffery orbit of a prolate axisymmetric ellipsoid (Jeffery 1922), and its size reduces as the major axis is tilted towards the flow vorticity direction. At $\theta_{tilt} = 0.5\pi$ (not shown in the figures), the vesicle is initially tilted such that its instantaneous major axis is parallel to the y-axis. The final orbit of the major axis reduces to two small loops around $(0, \pm1, 0)$, and the motion is nearly that of the out-of-plane TT. Unlike rigid ellipsoids, the vesicle's cross-section perpendicular to its major axis undergoes TR deformation instead of rigid body rotation. Hence, the trajectories of the two minor axes of the vesicle form simple closed figure '8' shapes, different from the doubly periodic trajectories of the minor axes of rigid ellipsoids (Hinch & Leal 1979).

In figure 24, we present results where the same initial condition is used as in figure 23(*a*), but at three different values of $\lambda = 11$, 10.5 and 10. At $\lambda = 11$, the orbit of the major axis (the one precessing about the y-axis) resembles that of a prolate ellipsoid despite the time variation of the axis length. At $\lambda = 10.5$, the shapes of those trajectories remain qualitatively the same but their sizes expand. A transition happens
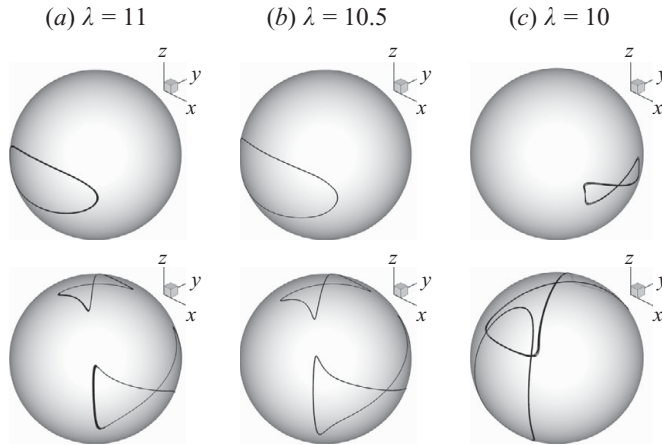
FIGURE 24. Trajectories of orientations of vesicles undergoing three-dimensional rotations. The flow parameters are labelled by '○' and '+' in the phase diagram of figure 23. The vesicle is initially tilted by $\theta_{tilt} = 0.3\pi$.

as λ is further reduced to 10; the major axis reverts to a figure '8'-shaped orbit around the x-axis. This is similar to the in-plane TR except that the axis is off the shear plane. The shortest axis on the other hand follows the 'O'-shaped orbit on the unit sphere, similar to an oblate ellipsoid. At $\lambda = 9$, the vesicle adopts the classical in-plane TR motion.

4. Conclusion and discussion

The motion of a model lipid vesicle in a simple shear flow is simulated with spectral surface resolution. Compared with the perturbation theory using high-degree harmonic expansion, we have found good agreement of the critical viscosity ratios for the transition from the in-plane tank-treading regime to the trembling and tumbling regimes. Fourth-degree harmonic expansions are necessary for quantitatively correct phase diagrams throughout the range of v-χ-λ considered; on the other hand, the stability boundaries obtained by fourth- and eighth-degree expansions only show minor differences.

Our linear stability analysis and DNS have revealed an out-of-plane tank-treading branch that is characterized by the alignment of the major axis with the vorticity direction. This branch is only stable when λ is above critical values. Below the critical viscosity ratio, the motion becomes unstable to perturbations that are non-symmetric about the shear plane. Furthermore, the numerical results demonstrate the existence of a broad class of three-dimensional time-periodic motion patterns that resemble the Jeffery orbit of rigid particles.

The rheology of dilute vesicle suspensions is studied systematically. We have found that the in-plane components of the non-dimensional particle specific stress are dominated by the resistance to the background shear flow, while the contribution from surface bending force is negligible at moderate and high shear rates. The non-monotonic dependence of particle shear stress on λ in the TT regime is shown to be the result of several competing factors: the decreasing inclination angle, the increase of the internal viscosity and the change of the axial lengths. The normal stress differences, especially the N_1/N_2 ratio, are significantly different from what is predicted by theory.

All numerical results obtained thus far demonstrate that the model vesicle ultimately follows either steady-state TT or one of the many time-periodic orbits. Vesicles in experiments however often exhibit shape oscillations of a broad spectrum, which can be attributed to membrane inhomogeneity and thermal fluctuations. These two factors are missing in the idealized model currently used and are of interest in our future investigation.

REFERENCES

ADAMS, J. C. & SWARZTRAUBER, P. N. 1997 SPHEREPACK 2.0: a model development facility. *NCAR Tech. Rep.*, NCAR/TN-436-STR.

BATCHELOR, G. K. 1970 The stress system in a suspension of force-free particles. *J. Fluid Mech.* **41**, 545–570.

BIBEN, T., FARUTIN, A. & MISBAH, C. 2009 Numerical study of 3D vesicles under flow: discovery of new peculiar behaviors. Available at: http://arxiv.org/abs/0912.4702v1.

BIBEN, T., KASSNER, K. & MISBAH, C. 2005 Phase-field approach to three-dimensional vesicle dynamics. *Phys. Rev.* E **72**, 041921.

DANKER, G., BIBEN, T., PODGORSKI, T., VERDIER, C. & MISBAH, C. 2007 Dynamics and rheology of a dilute suspension of vesicles: higher-order theory. *Phys. Rev.* E **76**, 041905.

DANKER, G. & MISBAH, C. 2007 Rheology of a dilute suspension of vesicles. *Phys. Rev. Lett.* **98**, 088104.

DESCHAMPS, J., KANTSLER, V. & STEINBERG, V. 2009 Phase diagram of single vesicle dynamical states in shear flow. *Phys. Rev. Lett.* **102**, 118105.

FARUTIN, A., BIBEN, T. & MISBAH, C. 2010 Analytical progress in the theory of vesicles under linear flow. *Phys. Rev.* E **81**, 061904.

FREUND, J. B. 2007 Leukocyte margination in a model microvessel. *Phys. Fluids* **19**, 023301.

GHIGLIOTTI, G., BIBEN, T. & MISBAH, C. 2010 Rheology of a dilute two-dimensional suspension of vesicles. *J. Fluid Mech.* **653**, 489–518.

HELFRICH, W. 1973 Elastic properties of lipid bilayers: theory and possible experiments. *Z. Naturforsch* C **28** (11), 693–703.

HINCH, E. J. & LEAL, L. G. 1979 Rotation of small non-axisymmetric particles in a simple shear flow. *J. Fluid Mech.* **92**, 591–608.

JEFFERY, G. B. 1922 The motion of ellipsoidal particles immersed in a viscous fluid. *Proc. R. Soc. Lond.* A **102**, 161–179.

KANTSLER, V. & STEINBERG, V. 2005 Orientation and dynamics of a vesicle in tank-treading motion in shear flow. *Phys. Rev. Lett.* **95**, 258101.

KANTSLER, V. & STEINBERG, V. 2006 Transition to tumbling and two regimes of tumbling motion of a vesicle in shear flow. *Phys. Rev. Lett.* **96**, 036001.

KAOUI, B., FARUTIN, A. & MISBAH, C. 2009 Vesicles under simple shear flow: elucidating the role of relevant control parameters. *Phys. Rev.* E **80**, 061905.

KELLER, S. R. & SKALAK, R. 1982 Motion of a tank-treading ellipsoidal particle in a shear flow. *J. Fluid Mech.* **120**, 27–47.

KIM, Y. & LAI, M. C. 2010 Simulating the dynamics of inextensible vesicles by the penalty immersed boundary method. *J. Comput. Phys.* **229**, 4840–4853.

KRAUS, M., WINTZ, W., SEIFERT, U. & LIPOWSKY, R. 1996 Fluid vesicles in shear flow. *Phys. Rev. Lett.* **77** (17), 3685–3688.

LEBEDEV, V. V., TURITSYN, K. S. & VERGELES, S. S. 2007 Dynamics of nearly spherical vesicles in an external flow. *Phys. Rev. Lett.* **99**, 218101.

LEBEDEV, V. V., TURITSYN, K. S. & VERGELES, S. S. 2008 Nearly spherical vesicles in an external flow. *New J. Phys.* **10**, 043044.

MADER, M., VITKOVA, V., ABKARIAN, M., VIALLAT, A. & PODGORSKI, T. 2006 Dynamics of viscous vesicles in shear flow. *Eur. Phys. J.* E **19**, 398–397.

MESSLINGER, S., SCHMIDT, B., NOGUCHI, H. & GOMPPER, G. 2009 Dynamical regimes and hydrodynamic lift of viscous vesicles under shear. *Phys. Rev.* E **80**, 011901.

MISBAH, C. 2006 Vacillating breathing and tumbling of vesicles under shear flow. *Phys. Rev. Lett.* **96**, 028104.

NOGUCHI, H. & GOMPPER, G. 2007 Swinging and tumbling of fluid vesicles in shear flow. *Phys. Rev. Lett.* **98**, 128103.

POZRIKIDIS, C. 1992 *Boundary Integral and Singularity Methods for Linearized Viscous Flow*. Cambridge University Press.

POZRIKIDIS, C. 2003 Numerical simulation of the flow-induced deformation of red blood cells. *Ann. Biomedical Engng* **31**, 1194–1205.

RALLISON, J. M. & ACRIVOS, A. 1978 A numerical study of the deformation and burst of a viscous drop in an extensional flow. *J. Fluid Mech.* **89**, 191–200.

SAAD, Y. & SCHULTZ, M. 1986 A generalized minimal residual algorithm for solving nonsymmetric linear systems. *SIAM J. Sci. Stat. Comput.* **7**, 856–869.

SEIFERT, U. 1999 Fluid membranes in hydrodynamic flow fields: formalism and an application to fluctuating quasispherical vesicles in shear flow. *Eur. Phys. J.* B **8**, 405–415.

SWARZTRAUBER, P. N. & SPOTZ, W. F. 2000 Generalized discrete spherical harmonic transforms. *J. Comput. Phys.* **159**, 213–230.

VEERAPANENI, S. K., GUEYFFIER, D., BIROS, G. & ZORIN, D. 2009a A boundary integral method for simulating the dynamics of inextensible vesicles suspended in a viscous fluid in 2D. *J. Comput. Phys.* **228**, 2334–2353.

VEERAPANENI, S. K., GUEYFFIER, D., BIROS, G. & ZORIN, D. 2009b A numerical method for simulating the dynamics of 3D axisymmetric vesicles suspended in viscous flows. *J. Comput. Phys.* **228**, 7233–7249.

VEERAPANENI, S. K., RAHIMIAN, A., BIROS, G. & ZORIN, D. 2011 A fast algorithm for simulating vesicle flows in three dimensions. *J. Comput. Phys.* (submitted).

VLAHOVSKA, P. M. & GRACIA, R. S. 2007 Dynamics of a viscous vesicle in linear flows. *Phys. Rev.* E **75**, 016313.

ZABUSKY, N. J., SEGRE, E., DESCHAMPS, J. & STEINBERG, V. 2010 Guide to phase diagrams for vesicles in shear and rotational flow: critique and future directions. Available at: http://arxiv.org/abs/1004.4733v1.

ZHAO, H., ISFAHANI, A. H. G., OLSON, L. & FREUND, J. B. 2010 A spectral boundary integral method for micro-circulatory cellular flows. *J. Comput. Phys.* **229** (10), 3726–3744.